Applied Catalysis B: Environmental 110 (2011) 40–49

Contents lists available at SciVerse ScienceDirect

Applied Catalysis B: Environmental

journal homepage: www.elsevier.com/locate/apcatb

Enhancement of catalytic properties for glycerol electrooxidation on Pt and Pd nanoparticles induced by Bi surface modification

Mário Simões, Stève Baranton, Christophe Coutanceau*

Equipe électrocatalyse, Laboratoire de Catalyse en Chimie Organique (LACCO), UMR 6503 CNRS, Université de Poitiers, 4 rue Michel brunet, B27, 86022 Poitiers cedex, France

ARTICLE INFO

Article history:
Received 23 June 2011
Received in revised form 29 July 2011
Accepted 18 August 2011
Available online 25 August 2011

Keywords:
Alkaline fuel cell
Bismuth
Glycerol
HPLC
In situ infrared spectroscopy
Palladium
Platinum

ABSTRACT

Effects toward electrocatalytic activity for glycerol oxidation of the modification of carbon supported Pd and Pt-based nanomaterials by bismuth were evaluated in alkaline medium. Pd/C, $Pd_{0.9}Bi_{0.1}$/C, Pt/C, $Pt_{0.9}Bi_{0.1}$/C and $Pd_{0.45}Pt_{0.45}Bi_{0.1}$/C catalysts were synthesized by a colloidal route, and physical and electrochemical methods were used to characterize the structure and the surface of the catalysts (TEM, HRTEM, EDX, XRD, ICP-OES and XPS). It was shown that only a few amount of bismuth was deposited on the Pt and/or Pd surface, and that no alloy was formed between bismuth and the other metals. The onset potential of glycerol oxidation is ca. 0.15 V lower on Pt/C than on Pd/C. However, Pt-free $Pd_{0.9}Bi_{0.1}$/C catalyst presented the same catalytic activity than platinum catalyst. The $Pt_{0.9}Bi_{0.1}$/C led reaching a higher catalytic activity by shifting the oxidation onset potential by ca. 0.2 V toward lower potentials compared with the Pt/C catalyst. But, the replacing of half of the platinum atoms by palladium atoms in the $Pd_{0.45}Pt_{0.45}Bi_{0.1}$/C material allowed achieving the same catalytic activity as with $Pt_{0.9}Bi_{0.1}$/C. Electrochemical experiments combined with *in situ* infrared spectroscopy measurements have shown that glycerol electrooxidation mechanism is independent on the catalyst, but dependent on the electrode potential. Chronoamperometry experiments combined with HPLC measurements showed that the main reaction products were glycerate, dihydroxyacetone and tartronate at low potentials, and that the increase of the electrode potential led to the formation of mesoxalate. For potential higher than 0.8 V *vs* RHE, the C–C bond cleavage occurred and oxalate and formiate were detected.

1. Introduction

Oxygenated species derived from glycerol have an important industrial interest [1]. Until now, many oxidation reactions are carried out by enzymatic processes or by using stoichiometric oxidants (e.g. permanganate, nitric acid or chromic acid) and these routes lead to the production of significant amounts of undesired byproducts. Therefore the utilization of oxygenated species derived from glycerol is still limited in an industrial scale and catalytic processes have to be developed [2,3]. However, glycerol oxidation follows a complex pathway of reactions that can lead to a large number of products [1].

The conversion of glycerol into oxygenated compounds having added value and/or industrial applications can be performed electrochemically [4]. In alkaline medium, palladium-based catalysts are active and stable for alcohol oxidation [5]. The modification of palladium or platinum surface by foreign atoms is known to greatly enhance their catalytic activity toward alcohol oxidation and to change their selectivity (and tolerance toward adsorbed poisoning species [4,6–8]). Amongst these foreign metals, bismuth is known to involve very important catalytic improvement in alkaline medium [9–15]. The study of the electrochemical behavior of platinum or palladium surfaces allowed increasing the understanding of the nature of the surface modifications and of the material structure [16–18].

The controlled synthesis of nanosized catalysts with surface properties similar to those of bulk compound surfaces is not trivial but is unavoidable in order to aim at industrial applications. Conversely to bulk platinum or palladium electrodes, few studies are dealing with the modification of palladium and platinum-based nanocatalysts by bismuth for the alcohol electrooxidation application. This aspect is one of the main goals of the present paper. For this purpose, Pd- and Pt-based nanoparticles modified by low atomic concentrations of bismuth are prepared by a colloidal route and deposited on a conductive carbon powder. The catalytic powders are characterized by physical and physicochemical methods (TEM, XRD, XPS, ICP-OES, TGA, and cyclic voltammetry) in order to determine their morphology, structure and composition. By combining physicochemical characterization, electrochemical performance of the catalytic

* Corresponding author. Tel.: +33 5 49 45 48 95; fax: +33 5 49 45 35 80.
E-mail address: christophe.coutanceau@univ-poitiers.fr (C. Coutanceau).

0926-3373/$ – see front matter © 2011 Elsevier B.V. All rights reserved.
doi:10.1016/j.apcatb.2011.08.020

materials, *in situ* spectroscopic determination of reaction intermediates and chromatographic measurements of reaction products, the present work brings new insights on the role of bismuth on electrocatalytic activity and selectivity toward the glycerol oxidation reaction as a function of catalyst composition and electrode potential.

2. Experimental

2.1. Catalyst synthesis by the "water-in-oil" microemulsion method

Catalysts were prepared by mixing $NaBH_4$ (99% from Acros Organics) as reducing agent, with a micro-emulsion carrying the metal salts dissolved in ultrapure water (MilliQ® Millipore, 18.2 MΩ cm). In particular, K_2PdCl_4, H_2PtCl_6, $6H_2O$ and $BiCl_3$ (from Alfa Aesar, 99.9%) were used. Polyethyleneglycol-dodecylether (BRIJ® 30 from Fluka) was chosen as surfactant and the organic phase was n-heptane (99% from Acros Organics). Desired amount of metal salts was dissolved in ultra-pure water in order to obtain metallic nanoparticles with controlled compositions. Carbon (Vulcan XC72), previously treated under N_2 at 400 °C for 4 h, was added directly in the colloidal solution to obtain the desired metal loading and the mixture was kept under stirring for 2 h. In the present work all the catalysts were synthesized in order to obtain 40 wt% metal loading after the reduction process with $NaBH_4$. The mixture was filtered on a 0.22 μm Durapore® membrane filter (Millipore). The resulting powder was abundantly rinsed with ethanol, acetone and ultra-pure water. The carbon-supported catalysts were dried overnight in an oven at 75 °C.

2.2. Physicochemical characterizations

Catalysts were characterized by transmission electron microscopy (TEM) using a JEOL 2100 UHR microscope (200 kV) equipped with a LaB_6 filament. Images were taken with a Gatan Ultrascan 2k × 2k camera. The mean particle size and size distributions were determined by measuring the diameter of isolated particles using ImageJ free software [19], although particle agglomeration is present in all catalysts. Between 200 and 300 particles were considered for each catalyst in order to have an acceptable statistical sample. The microstructure of the catalytic powders was evaluated by X-ray diffraction (XRD). The powder diffraction patterns were recorded on a Bruker D5005 Bragg–Brentano (θ–θ) diffractometer operated with a copper tube powered at 40 kV and 40 mA (unfiltered $CuK_{\alpha 1}$ = 1.542 Å). Measurements were recorded from $2\theta = 15°$ to $2\theta = 90°$ in step mode, with steps of 0.06° and a fixed acquisition time of 10 s/step. Oxidation states and possible electronic interactions between metals were evaluated by X-ray photoelectron spectroscopy (XPS). Spectra were collected using a VG ESCALAB 3 MKII spectrometer using a monochromatized Mg K_α radiation (1253.6 eV). The source was operated at 300 W (15 kV and 20 mA). Powder analysis covered a surface of 2 mm × 3 mm. XPS spectra were calibrated with respect to the C 1s orbital at 284.6 eV.

Thermogravimetric measurements were carried out with a TA Instrument SDT Q600 apparatus. A few milligrams of catalytic powder was put in an alumina crucible and heated under air from 25 °C to 900 °C. Different temperature slopes were used according to the temperature range: 10 °C min^{-1} from 25 °C to 400 °C, then 2 °C min^{-1} from 400 °C to 600 °C and 10 °C min^{-1} from 600 °C to 900 °C.

The catalyst compositions were determined using an inductive coupling plasma-optical emission spectrometer (ICP-OES Perkin-Elmer Optima 2000 DV).

2.3. Electrochemical characterizations

Catalytic powders were deposited on a glassy carbon substrate according to a method proposed by Gloaguen et al. [20]. The catalytic powder (25 mg) was added to a mixture of 0.5 mL Nafion® solution (5 wt% from Aldrich) in 2.5 mL ultra-pure water. After ultrasonic homogenization of the catalyst/XC72-Nafion® ink, a given volume was deposited from a syringe onto a fresh polished glassy carbon substrate yielding a catalytic powder loading of 354 μg cm^{-2} (141.6 μg_{metal} cm^{-2}) with 21.85 μg cm^{-2} of Nafion (6 wt%), leading to a catalytic layer thickness in the range from 1 to 1.5 μm [21,22]. The solvent was then evaporated in a stream of pure nitrogen at room temperature. The electrochemical set-up consisted in a computer controlled Voltalab PGZ 402 potentiostat. The solutions were prepared from NaOH (Semiconductor Grade 99.99%, Sigma–Aldrich), glycerol (Reagent Plus ≥99%, Sigma–Aldrich) and ultra-pure water (18.2 MΩ cm). The electrochemical experiments were carried out at 20 °C in N_2-purged supporting electrolyte, using a conventional thermostated three-electrode electrochemical cell. The working electrode was a glassy carbon disk (0.071 cm^2 geometric surface area), the counter electrode was a glassy carbon plate (8 cm^2 geometric surface area) and the reference electrode was a Reversible Hydrogen Electrode (RHE).

A qualitative analysis of glycerol electrooxidation products was performed at different electrode potentials using a Dionex HPLC set-up, fitted with an ASI 1000 Automated Sample Injector, a P680 HPLC pump (flow rate of 0.6 mL min^{-1}) and a 300 mm length Aminex® HPX-87 column. The eluent was a 8×10^{-3} mol L^{-1} H_2SO_4 aqueous solution and the detection was ensured by a refraction index detector (IOTA 2 from Precision Scientific). Reference solutions for the determination of expected reaction products were aqueous solutions of NaOH 0.1 mol L^{-1} + 10^{-2} mol L^{-1} of products.

3. Results and discussion

3.1. Physicochemical and electrochemical characterizations

The physicochemical characterizations of the Pt/C, Pd/C, $Pd_{0.9}Bi_{0.1}$/C, $Pt_{0.9}Bi_{0.1}$/C and $Pd_{0.45}Pt_{0.45}Bi_{0.1}$/C are reported in Table 1. Main results of TGA measurements indicate that metal loadings are close to the 40 wt% nominal one, in the range from 36 wt% to 38 wt%. The bulk composition of catalysts determined by ICP-OES is also consistent with the desired ones. TEM analyses presented in Fig. 1a–e showed that the presence of bismuth led to the increase of the mean particle size of palladium based nanomaterials (of ca. 1.2 nm), from 4.0 nm to 5.2 nm for Pd/C and $Pd_{0.9}Bi_{0.1}$/C, respectively, whereas it has no significant effect on the mean size for Pt/C and $Pt_{0.9}Bi_{0.1}$/C catalysts with ca. 5.0 nm in both cases. The trimetallic catalyst $Pd_{0.45}Pt_{0.45}Bi_{0.1}$/C (Fig. 1e) displays a mean particle size of ca. 4.5 nm, lying between those of Pd and Pt monometallic ones. Nano-EDX analyses performed on isolated particles showed that the three metals were present in the particles (Fig. 1f). Although the presence of agglomerates for all catalysts was observed, nanoparticles were disseminated homogeneously on the carbon support. However, low magnification TEM photographs (not shown) pointed out the presence of zones which were found to be mainly composed by bismuth according to EDX analyses.

XRD measurements were performed to determine the microstructure of the mono-, bi- and tri-metallic materials. XRD patterns are given in Fig. 2. Analyses of the diffractograms allowed determining the cell parameters using the Bragg equation [23] and indicated that the $Pd_{0.9}Bi_{0.1}$/C and $Pt_{0.9}Bi_{0.1}$/C present the typical fcc crystalline structure of palladium and platinum, respectively. Concerning the tri-metallic catalyst, the narrow gap between the peak position of Pt and Pd in the diffractogram did not

Table 1
Physicochemical characterization data obtained for the different materials; metal loadings are determined from TGA measurements, cell parameter (a) and Scherrer lengths (L_v) from XRD patterns, particle sizes d_{TEM} from TEM pictures and metal ratios from ICP-OES measurements.

	Metal loading (wt%)	Cell parameter a (nm)	Scherrer length L_v (nm)	Particle size d_{TEM} (nm)	Metal ratio (at%)		
					at% Pd	at% Pt	at% Bi
Pd/C	36	0.3938	4.1	4.0	100	–	–
Pt/C	37	0.3942	5.5	5.3	–	100	
$Pd_{0.9}Bi_{0.1}/C$	38	0.3938	4.5	5.2	92	–	8
$Pt_{0.9}Bi_{0.1}/C$	36	0.3943	5.7	4.7	–	90	10
$Pd_{0.45}Pd_{0.45}Bi_{0.1}/C$	38	0.3943	4.7	4.5	43	45	12

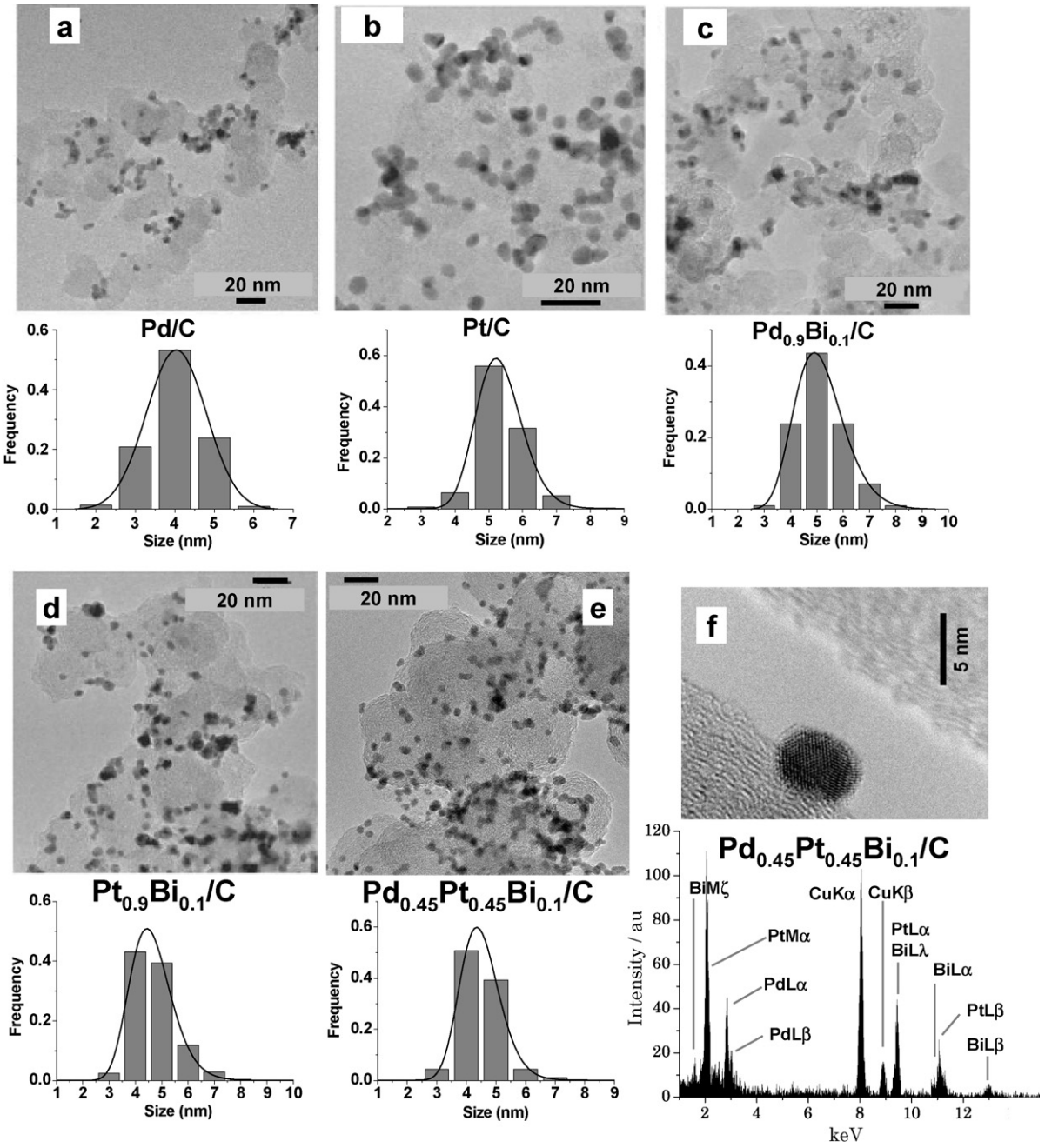

Fig. 1. (a)–(e) TEM images and size distributions for the different synthesized catalysts. (f) HRTEM image of a single nanoparticle from the $Pd_{0.45}Pt_{0.45}Bi_{0.1}/C$ catalytic powder and nano-EDX measurement spectrum recorded on this particle.

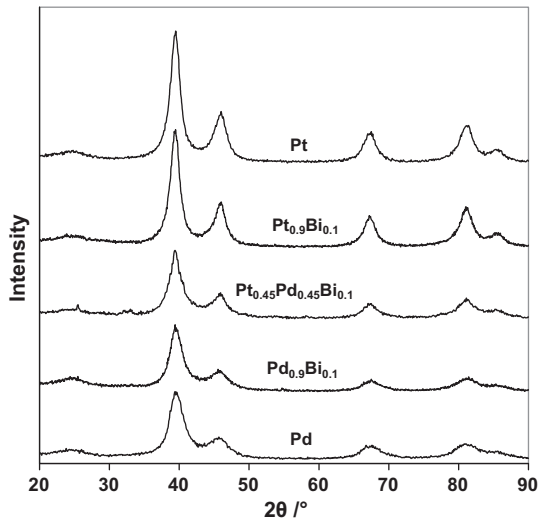

Fig. 2. XRD diffraction patterns of the Pd, Pt and Bi-based catalysts (40 wt% metal loading on carbon).

allow using the Vegard's law to determine the degree of alloying of both metals. However, the analysis of the XRD measurement carried out on the tri-metallic material indicated that it presents the fcc structure with small diffraction peaks that have arisen, due to the presence of unalloyed bismuth species (most probably isolated from platinum–palladium particles).

XPS measurements were carried out on the Pt/C, Pd/C, $Pd_{0.9}Bi_{0.1}$/C, $Pt_{0.9}Bi_{0.1}$/C and $Pd_{0.45}Pt_{0.45}Bi_{0.1}$/C samples to determine the surface compositions, the oxidation states and the eventual interactions between the different elements in the materials. The spectrum analysis is based on data obtained from the "Handbook of X-ray Photoelectron Spectroscopy" [24]. Table 2 summarizes the main results. XPS spectra are presented in Fig. 3a–i. In the case of Pd/C material, the 3d core level spectrum of palladium displays two asymmetrical peaks separated by 5.3 eV related to Pd $3d_{5/2}$ and Pd $3d_{3/2}$ orbitals. The signals of Pd $3d_{5/2}$ could be decomposed into 2 peaks, one centered at 336.4 eV assigned to PdO and a second peak centered at 337.6 eV assigned to the presence of PdO_2: no metallic Pd was detected which indicates that the nanomaterial is under its oxidized form. In the $Pd_{0.9}Bi_{0.1}$/C XPS spectrum on the binding energy range corresponding to Pd $3d_{5/2}$ and Pd $3d_{3/2}$ orbitals, the positions of the peaks are shifted from ca. 1 eV toward lower binding energy compared to XPS spectrum recorded on Pd/C catalyst. The peaks measured at 335.7 eV and 336.8 eV were related to metallic palladium and PdO, respectively, i.e. to Pd species with globally lower oxidation states than for the Pd/C material. The 4f core level spectrum of Bi is composed of two peaks separated by 5.4 eV, corresponding to the Bi $4f_{7/2}$ and Bi $4f_{5/2}$ orbitals. The fitting of the Bi $4f_{7/2}$ signal led to two peaks centered at 158.9 eV and 159.4 eV, which were attributed to Bi_2O_3 and $Bi(OH)_3$ species [17,24], respectively.

In the case of the Pt/C monometallic material, the Pt $4f_{7/2}$ asymmetrical peak (separated by 3.35 eV from that of Pt $4f_{5/2}$ peak) was fitted with two peaks located at 71.3 eV and 72.2 eV. The first one was assigned to metallic platinum and the second one to $Pt(OH)_2$ species. In presence of Bi, platinum displayed the same oxidation state as in the monometallic Pt/C material. However, the atomic ratio of platinum under $Pt(OH)_2$ form is lower in the $Pt_{0.9}Bi_{0.1}$/C catalyst than in the Pt/C catalyst. Moreover, the XPS analysis of the $Pt_{0.9}Bi_{0.1}$/C material showed a lower oxidation state of Bi in presence of Pt. Electronic interactions between bismuth and palladium or platinum are then clearly evidenced. XPS spectra recorded for the $Pd_{0.45}Pt_{0.45}Bi_{0.1}$/C are given in Fig. 3g–i. In this catalyst, palladium

Table 2
XPS characterization data obtained for the different materials; binding energy values for the maximum of XPS peaks relate to Pd $3d_{5/2}$, Bi $4f_{7/2}$ and, Pt $4f_{7/2}$, related possible compounds in the catalytic phases, element (Pd, Pt, Bi, C and O) atomic ratios in the catalytic powder obtained from XPS peak areas and metal composition of catalysts determined from XPS data.

	XPS peak position			Compound	Element atomic ratio					Metal composition (at%)
	Pd $3d_{5/2}$ (eV)	Bi $4f_{7/2}$ (eV)	Pt $4f_{7/2}$ (eV)		Pd (at%)	Bi (at%)	Pt (at%)	O (at%)	C (at%)	
Pd/C	336.4	–	–	PdO	1.58	–	–	14.4	80.89	Pd_1
	337.6	–	–	PdO_2	3.13	–	–			
Pt/C	–	–	71.3	Pt	–	–	1.29	6.24	90.76	Pt_1
	–	–	72.2	$Pt(OH)_2$	–	–	1.72			
$Pd_{0.9}Bi_{0.1}$/C	335.7	–	–	Pd	0.79	–	–	8.19	89.34	$Pd_{0.84}Bi_{0.16}$
	336.8	–	–	PdO	1.29	–	–			
	–	158.9	–	Bi_2O_3	–	0.25	–			
	–	159.4	–	$Bi(OH)_3$	–	0.14	–			
$Pt_{0.9}Bi_{0.1}$/C	–	–	71.5	Pt	–	–	1.37	5.64	91.72	$Pt_{0.89}Bi_{0.11}$
	–	–	72.6	$Pt(OH)_2$	–	–	0.99			
	–	157.7	–	Bi	–	0.09	–			
	–	158.3	–	Bi_2O_3	–	0.2	–			
$Pd_{0.45}Pt_{0.45}Bi_{0.1}$/C	335.8	–	–	Pd	0.85	–	–	8.93	87.09	$Pd_{0.40}Pt_{0.43}Bi_{0.17}$
	336.7	–	–	PdO	0.74	–	–			
	–	158.6	–	Pt	–	0.52	–			
	–	160.4	–	$Pt(OH)_2$	–	0.14	–			
	–	–	71.6	Bi_2O_3	–	–	0.96			
	–	–	72.7	$Bi(OH)_3$	–	–	0.77			

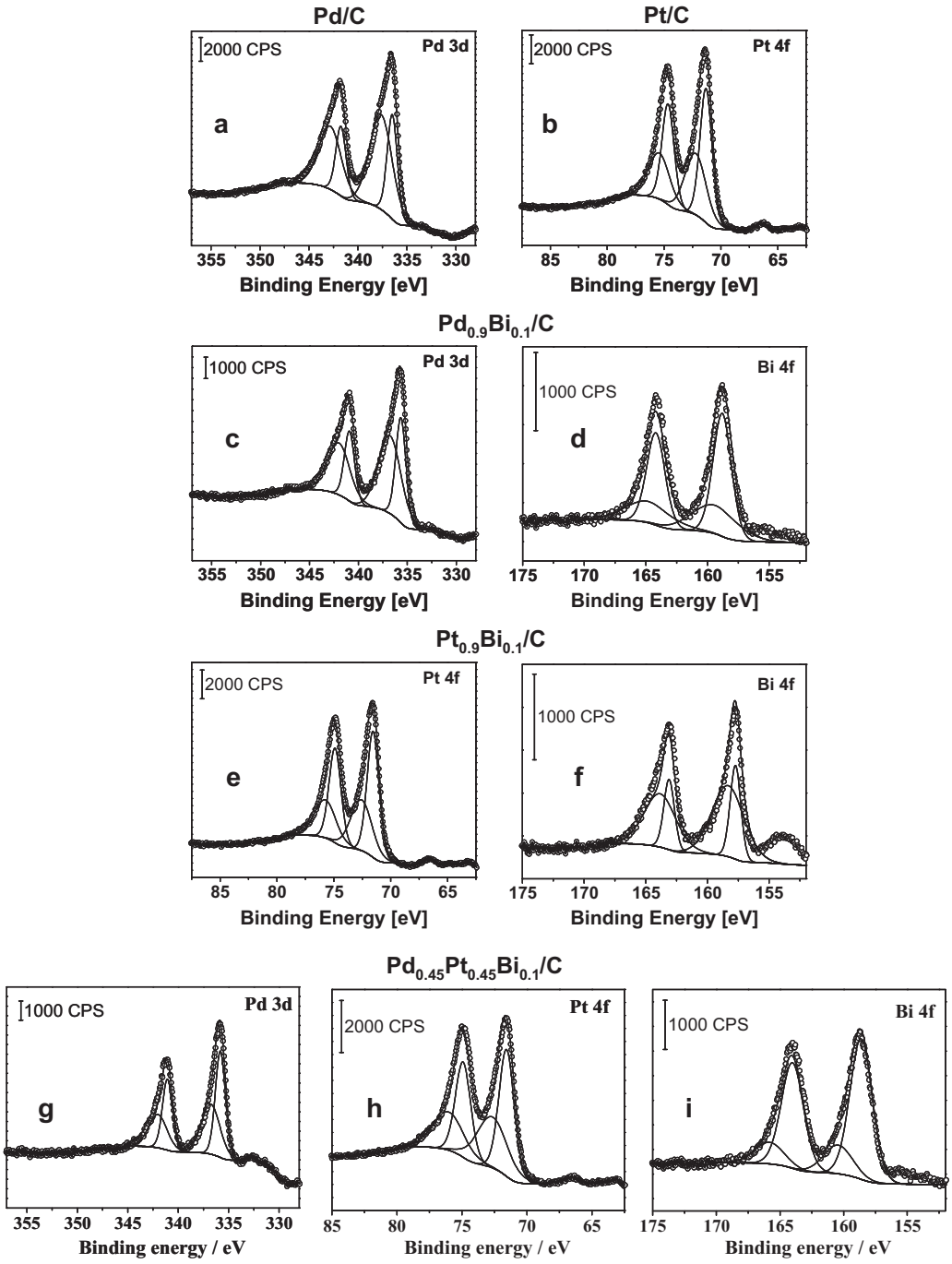

Fig. 3. Detailed XPS spectra for Pd 3d, Pt 4f and Bi 4f orbital on synthesized catalysts (a) Pd/C; (b) Pt/C; (c–d) $Pd_{0.9}Bi_{0.1}/C$; (e–f) $Pt_{0.9}Bi_{0.1}/C$ and (g–i) $Pd_{0.45}Pt_{0.45}Bi_{0.1}/C$.

and platinum presented same oxidation states than those determined on $Pd_{0.9}Bi_{0.1}/C$ and $Pt_{0.9}Bi_{0.1}/C$ materials, whereas bismuth appeared to be globally more oxidized than in the $Pt_{0.9}Bi_{0.1}/C$ catalyst. The electronic interaction between palladium and platinum could influence that between bismuth and both these metals.

The determination by XPS of the concentration of bismuth in the surface atomic layers gave values that are always a little bit higher than that for bulk composition determined by ICP-OES or nano-EDX. Bismuth is certainly mainly disseminated within the surface atomic layers of nanoparticles, which is in agreement with results from Kimura et al. [13] concerning the interaction of Pt(1 1 1) with bismuth. It can then be proposed that bismuth is mainly present at the catalyst surface. Considering the mean escape depth of photoelectrons, close to 1 nm across platinum for example [25,26], and the mean particle diameter (close to 5 nm), it is likely that all atoms in palladium or platinum based nanoparticles, from the surface to the center, may be involved in the global XPS signal. However, an enhancement of the signal due to species present at the surface of nanoparticles can be expected. This hypothesis led to the interpretation that the slight increase of the amount of bismuth determined by XPS analysis when compared with ICP-OES or EDX analysis, results from the presence of bismuth on platinum or palladium particle surface.

Voltammograms of Pd/C and $Pd_{0.9}Bi_{0.1}/C$ materials recorded in supporting electrolyte are presented in Fig. 4a. Comparing the cyclic voltammograms, the presence of bismuth inhibits the adsorption–absorption/reaction of hydrogen on palladium, since peaks in the potential region from 0.4 to 0.6 V *vs* RHE recorded on

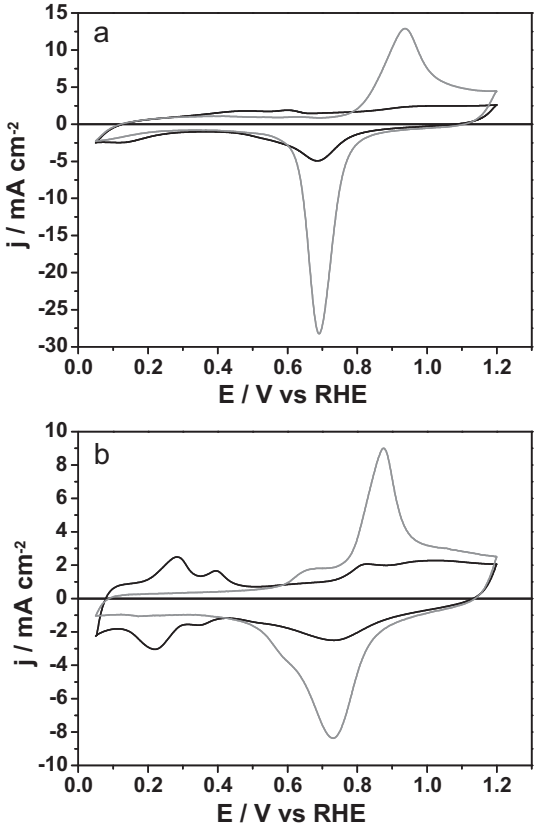

Fig. 4. Cyclic voltammograms of (a) Pd/C (black line) and $Pd_{0.9}Bi_{0.1}$/C (grey line) catalysts and (b) Pt/C (black line) and $Pt_{0.9}Bi_{0.1}$/C (grey line) catalysts ($\nu = 50\,mV\,s^{-1}$, N_2-saturated, 1 mol dm^{-3} NaOH electrolyte, $T = 293\,K$).

the $Pd_{0.9}Bi_{0.1}$/C surface are smaller than those recorded on Pd/C. Those peaks are related to interactions between hydrogen and Pd(1 1 1) and Pd(1 0 0), respectively [27]. Casella and Contursi [17] verified a similar effect on palladium electrodes modified by bismuth adatoms. At higher potentials, an oxidation current starts to appear from ca. 0.7 V *vs* RHE which is related to the palladium surface oxidation [28]. Then, an intense oxidation peak located at ca. 0.9–0.95 V *vs* RHE was assigned to surface oxidation processes of bismuth. During the negative going scan, the reduction peak located at ca. 0.7 V on the $Pd_{0.9}Bi_{0.1}$ catalyst was assigned to the simultaneous reduction of Pd and Bi oxides [17], which confirms the electronic interaction between both metals as suggested by XPS measurements.

Comparing the voltammograms of Pt/C and $Pt_{0.9}Bi_{0.1}$/C materials in alkaline medium given in Fig. 4b, the presence of bismuth led again to inhibit the adsorption reaction of hydrogen on platinum, in agreement with other studies performed on bulk electrodes [16,29]. The surface oxidation starts at lower potential on $Pt_{0.9}Bi_{0.1}$/C catalyst than on the Pt/C one. Two quasi-reversible oxidation/reduction peaks are visible in the voltammogram of $Pt_{0.9}Bi_{0.1}$/C at ca. 0.75 V and 0.95 V *vs* RHE. The first peak at 0.75 V was previously attributed to the oxidation of bismuth disseminated on the carbon surface, whereas the peak at higher potential was assigned to the oxidation of bismuth at the platinum surface [30].

The voltammogram of $Pd_{0.45}Pt_{0.45}Bi_{0.1}$/C in alkaline medium (Fig. 5) seems to indicate that the surface oxidation followed the same mechanism as that proposed for the $Pt_{0.9}Bi_{0.1}$/C material; although the bismuth oxidation current of the peak located at ca. 0.9 V *vs* RHE is higher than that recorded on the $Pt_{0.9}Bi_{0.1}$/C catalyst, being close to that recorded on the $Pd_{0.9}Bi_{0.1}$/C catalyst. The influence of bismuth on $Pd_{0.5}Pt_{0.5}$ bimetallic particles is very similar to

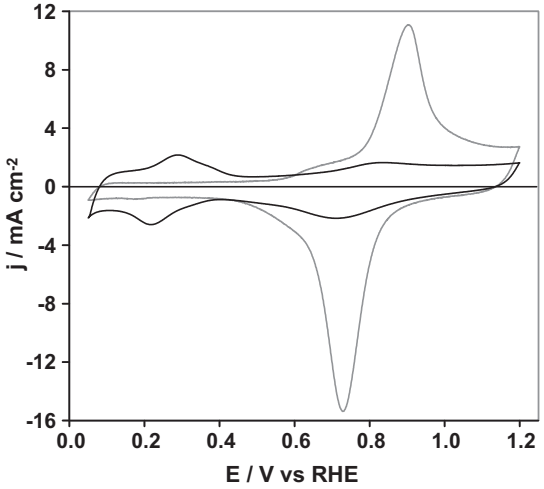

Fig. 5. Cyclic voltammograms of a $Pd_{0.45}Pt_{0.45}Bi_{0.1}$/C catalyst ($\nu = 50\,mV\,s^{-1}$, N_2-saturated, 1 mol dm^{-3} NaOH electrolyte, $T = 293\,K$).

that observed with the $Pd_{0.9}Bi_{0.1}$/C and $Pt_{0.9}Bi_{0.1}$/C, inhibiting the hydrogen adsorption/absorption processes. This clearly indicates that bismuth is mainly disseminated at the nanoparticle surface and is in interaction with Pd and Pt.

3.2. Electrochemical activity and selectivity toward the glycerol oxidation

The polarization curves recorded in glycerol 0.1 mol dm^{-3} + NaOH 1.0 mol dm^{-3} solution during the third voltammetric cycle are given in Fig. 6a and b. The glycerol oxidation on Pd/C catalyst starts at a potential of ca. 0.5 V *vs* RHE, which is a potential ca. 0.1 V higher than that observed on Pt/C material. Both catalysts deactivate for potentials higher than 0.9 V due to surface oxide formation. This last behavior was observed with all studied catalysts. The $Pd_{0.9}Bi_{0.1}$/C catalyst displays a higher activity than the Pd/C one, reaching that of the Pt/C catalyst. The onset potential of the oxidation wave is ca. 0.4 V *vs* RHE. The current density values recorded between 0.5 V and 0.8 V *vs* RHE are also higher than those observed on the Pd/C material. Higher kinetics for the glycerol electrooxidation is clearly achieved with $Pd_{0.9}Bi_{0.1}$/C than with Pd/C. The modification of platinum leads to an important increase of the catalytic activity toward glycerol oxidation, since the onset potential on the $Pt_{0.9}Bi_{0.1}$/C catalyst is shifted by ca. 0.2 V toward lower potentials in comparison with that observed on the Pt/C catalyst. Again, higher current densities are recorded over the whole potential range where the platinum-based catalysts are active. At last, the onset potential of glycerol electrooxidation on the trimetallic $Pd_{0.45}Pt_{0.45}Bi_{0.1}$/C catalyst is the same as with the $Pt_{0.9}Bi_{0.1}$/C, but higher current densities are recorded from ca. 0.5 to ca. 0.9 V *vs* RHE, whereas 50% of platinum atoms are replaced by palladium atoms. The activity enhancement induced by small addition of bismuth to Pt and/or Pd nanoparticles could be explained by changes in the electronic interactions between the reactant and the active sites of the catalyst [31,32], by the bifunctional mechanism [33] and/or by the ensemble effect [34]. Modification of platinum and/or palladium surface by adatoms not only can improve the activity of alcohol oxidation, but also affect the composition of chemisorbed species and further the selectivity of catalysts [35,36].

In order to shed light on the influence of physicochemical structure of the catalytic surface on reaction mechanisms, *in situ* infrared spectroscopy experiments were carried out at low potential scan rate. Infrared spectra as a function of the electrode potential were

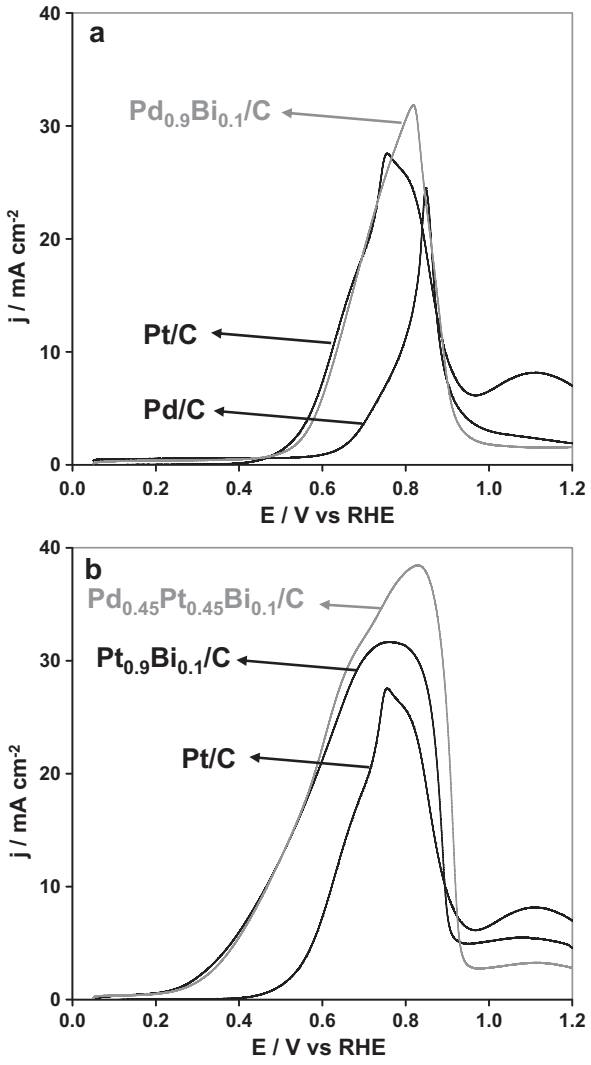

Fig. 6. Polarization curves of glycerol oxidation recorded on (a) Pt/C, Pd/C, $Pd_{0.9}Bi_{0.1}$/C and (b) Pt/C, $Pt_{0.9}Bi_{0.1}$/C and $Pd_{0.45}Pt_{0.45}Bi_{0.1}$/C ($v$ = 10 mV s^{-1}, N_2-saturated, 0.1 mol dm^{-3} glycerol + 1.0 mol dm^{-3} NaOH electrolyte, T = 293 K).

recorded every 0.05 V during linear potential scan from 0.05 V *vs* RHE to 1.2 V *vs* RHE in a 0.1 mol dm^{-3} glycerol, 1.0 M NaOH electrolyte. However for a better readability, only spectra recorded every 0.1 V between 0.05 and 1.15 V *vs* RHE are presented in Fig. 7a–e. In previous *in situ* infrared studies of glycerol electrooxidation on Pt/C, Pd_xAu_{1-x}/C and Au/C catalysts [4], we proposed that pure Pt and Pd-based nanomaterials led to the same glycerol oxidation reaction pathway, as same infrared absorption peaks appeared for both catalysts (Fig. 7a and b), whereas on Au/C two mechanism pathways were identified, one via the formation of glyceraldehyde and glycerate ions (called route A) and the other via the formation of hydoxypyruvate (called route B).

Spectra recorded on $Pd_{0.9}Bi_{0.1}$/C and $Pt_{0.9}Bi_{0.1}$/C catalysts in Fig. 7c and d do not show the absorption band at 1900 cm^{-1} and 1950 cm^{-1}, respectively, related to surface CO on palladium [37], which is present on the Pd/C and Pt/C catalysts (Fig. 7a). This indicates that the glycerol adsorption on the $Pd_{0.9}Bi_{0.1}$/C and $Pt_{0.9}Bi_{0.1}$/C materials is not dissociative, which can be correlated to the presence of bismuth at the palladium and platinum surface. Except for this behavior, the glycerol oxidation on bismuth containing materials occurs according to the same reaction pathway as with Pd/C and Pt/C catalysts. The absorption band D (assigned to dihydroxyacetone [38]) appears as soon as the oxidation onset potential is reached, although the reaction continues via the primary alcohol oxidation; indeed bands C (ca. 1310 cm^{-1}), E (ca. 1385 cm^{-1}) and F (ca. 1575 cm^{-1}) correspond to glyceraldehyde or glycerate ion C–O stretching and glycerate ion COO^- stretching, respectively [38]. *In situ* infrared measurements indicated that the reaction mechanism on $Pd_{0.9}Bi_{0.1}$/C followed the route A as for the Pd/C materials, and therefore that modification of palladium by bismuth only led to higher activity and not to a change in selectivity.

For both PdBi and PtBi catalysts, the formation of $Bi(OH)_3$ species according to Eq. (1) at relatively low potentials leads to increase the hydroxyl ions concentration at the vicinity of the surface, and further to the enhancement of the oxidation reaction activity.

$$Bi + 3OH^- \rightarrow Bi(OH)_3 + 3e^- \quad (1)$$

The importance of keeping appropriate concentration of hydroxyl species in the case of glycerol oxidation on Au electrode surface has indeed been recently pointed out by Jeffery and Camara [39].

At the beginning of the oxidation reaction, at low potentials, the formation of the dihydroxyacetone species is favored (band D), indicating that the secondary alcohol function is oxidized first on these catalysts. The presence of bismuth on the catalytic metal surface changes the absorption mode of glycerol, leading to inhibit the glycerol dissociation at low potentials. For higher potentials, absorption bands C and E, assigned to carboxylate groups coming from primary alcohol oxidation of glycerol, appears at the expense of absorption band D. Moreover, the position of absorption band F is shifted with the change in the reaction mechanism. At low potentials, when the product characterized by the absorption band D is the main product formed at the electrode, the absorption band F is centered at 1580 cm^{-1}, whereas at higher potentials, when the product characterized by the presence of absorption bands C and E becomes the most important, the absorption band F is shifted toward 1570 cm^{-1}. The glycerol oxidation reaction appears then very dependent on the electrode potential. These catalysts seem to favor the route B at low potentials (oxidation of the secondary alcohol); then a change in the reaction mechanism occurs at higher potentials leading to favor the route A. The increase of the electrocatalytic activity with respect to the monometallic catalysts can be attributed to a synergetic effect between the catalytic metal and bismuth and to the bifunctional mechanism. First, the presence of bismuth inhibits the dissociative adsorption of glycerol which leads to the decrease of the surface poisoning by adsorbed CO species. Furthermore, the oxidation of the secondary alcohol group occurs in a different potential range than that of the primary alcohol groups. This shows clearly that the presence of bismuth has an influence on the adsorption mode of glycerol. The oxidation of bismuth at high potentials, leading to the increase of hydroxyl species concentration, allows completing the oxidation reaction by maintaining a high pH at the vicinity of the electrode.

The *in situ* infrared spectra recorded on $Pd_{0.45}Pt_{0.45}Bi_{0.1}$/C are presented in Fig. 7e. Two absorption bands, at 1225 cm^{-1} (absorption band B) and 1335 cm^{-1} (absorption band C′), appear at low potentials, which are assigned to C–O stretching (aldehyde polymers or alcohols) and C–O stretching (glyceraldehyde or glycerate ion) [38]. It seems that the first reaction step of the glycerol oxidation mechanism involves glyceraldehyde species; the absorption band D corresponding to hydroxyacetone appears then. The glyceraldehyde species has not been detected before on bismuth-containing catalysts. We explain this by the existence of an equilibrium between isomers, glyceraldehyde and dihydroxyacetone. If the oxidation reaction kinetics is much higher than that of the isomerization reaction, then the detection of the aldehyde by the SPAIR technique becomes very difficult. Therefore, it appears that the mechanisms of glycerol electrooxidation are similar to those proposed on the other Bi-containing catalysts. At low

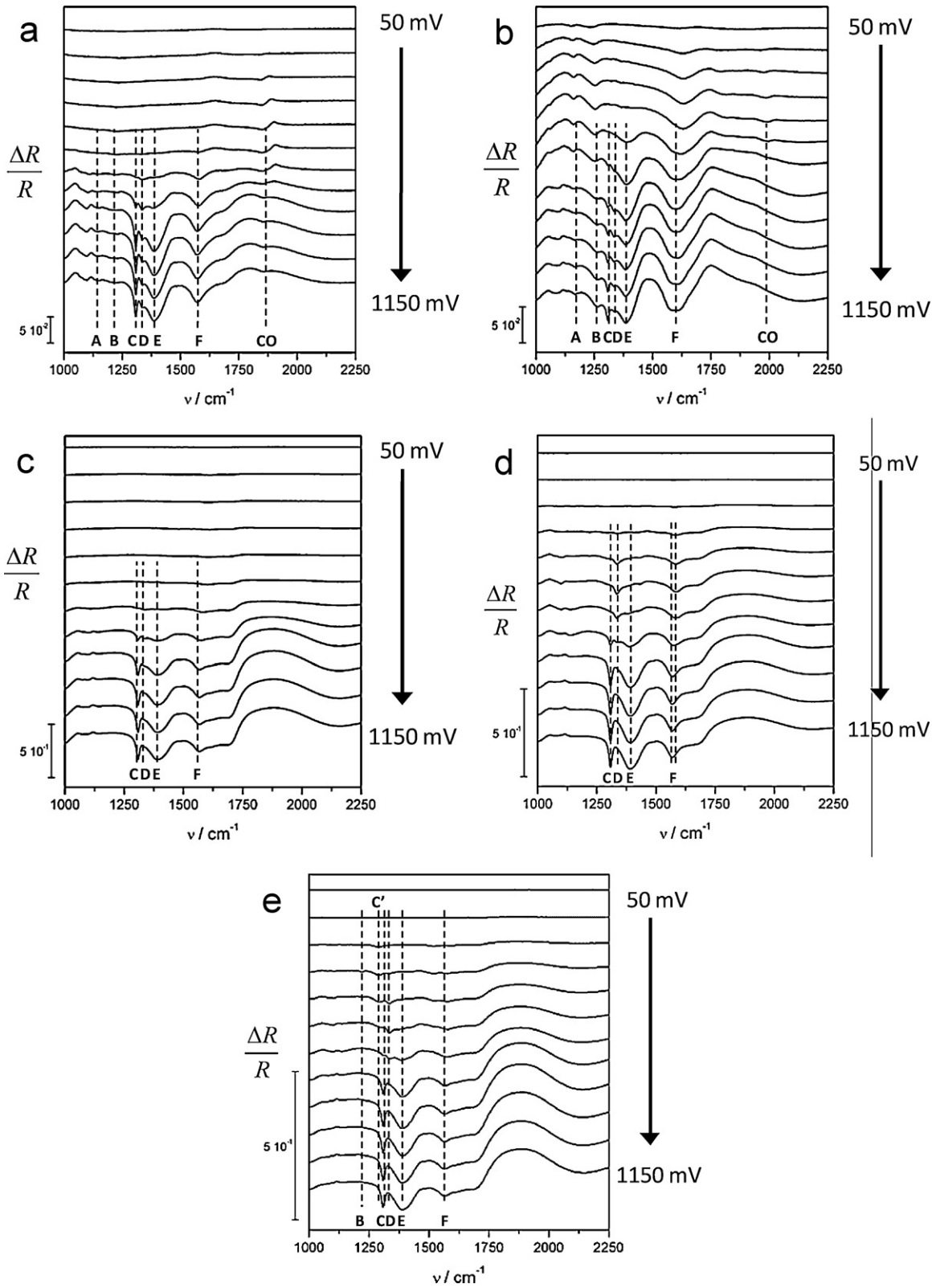

Fig. 7. Infrared spectra recorded during glycerol oxidation on (a) Pd/C, (b) Pt/C, (c) $Pd_{0.9}Bi_{0.1}$/C, (d) $Pt_{0.9}Bi_{0.1}$/C and (e) $Pd_{0.45}Pt_{0.45}Bi_{0.1}$/C catalysts in 0.1 mol dm^{-3} glycerol, 1.0 mol dm^{-3} NaOH electrolyte at 293 K. Scan rate: 1 mV s^{-1}, resolution 4 cm^{-1}.

and intermediate potentials, the formation of dihydroxyacetone is favored, and for higher potentials the preferential oxidation of primary alcohol groups occurs.

The mechanistic analysis has been completed by the determination of reaction product by HPLC after chronoamperometric experiments. The glycerol oxidation is performed at a constant electrode potential, for a long enough period of time to ensure a glycerol conversion yield of ca. 50%. Table 3 presents the products detected by HPLC as a function of the electrode potential for the different catalysts. The studied potential range was determined

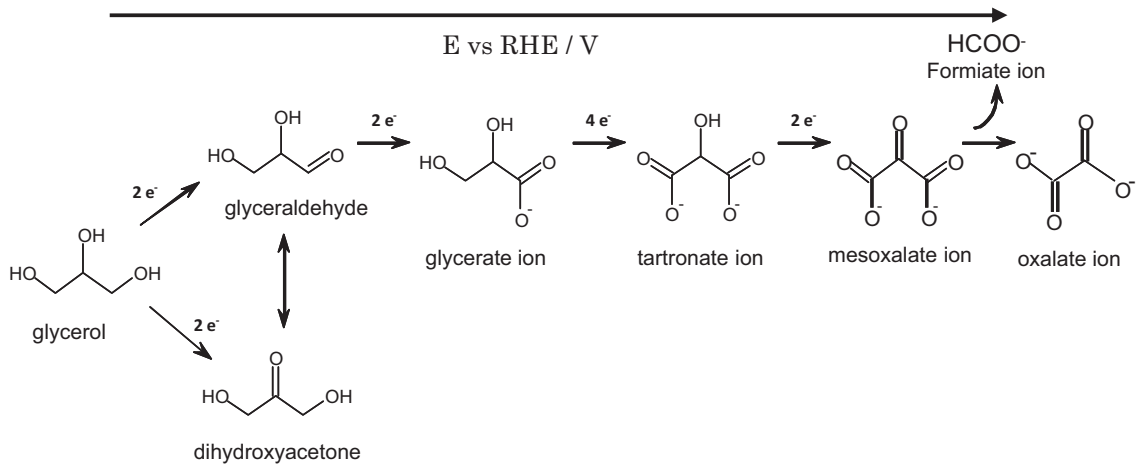

Scheme 1. Reaction mechanism proposed for the electrooxidation of glycerol on $Pd_{0.9}Bi_{0.1}/C$, $Pt_{0.9}Bi_{0.1}/C$ and $Pd_{0.45}Pt_{0.45}Bi_{0.1}/C$ catalysts.

Table 3
Oxidation products detected by HPLC after chronoamperometry experiments at different potentials in glycerol 0.1 mol dm^{-3} + NaOH 1 mol dm^{-3} deaerated electrolyte at T = 20 °C (Glyt: glycerate ion; Dihyd: dihydroxyacetone; Tar: tartronate ion; Mesox: mesoxalate ion; Oxal: oxalate ion; and Form: formiate ion).

Catalysts	E/V *vs* RHE	Products detected by HPLC				
$Pd_{0.45}Pt_{0.45}Bi_{0.1}/C$	0.25	Glyt/Dihyd	Tar			
	0.45	Glyt/Dihyd	Tar			
	0.60	Glyt/Dihyd	Tar	Mesox		
	0.80	Glyt/Dihyd	Tar	Mesox		
$Pt_{0.9}Bi_{0.1}/C$	0.55	Glyt/Dihyd	Tar			
	0.85	Glyt/Dihyd	Tar	Mesox	Oxal	Form
$Pd_{0.9}Bi_{0.1}/C$	0.85	Glyt/Dihyd	Tar	Mesox	Oxal	Form

according to the results obtained from *in situ* infrared study.

The $Pd_{0.45}Pt_{0.45}Bi_{0.1}/C$ is the material displaying the lower overpotential for the glycerol electrooxidation reaction. The product distribution at 0.25 V *vs* RHE (glycerate and dihydroxyacetone) indicates that glycerol oxidation occurs by an attack of the primary alcohol groups. No glyceraldehyde was detected, which seems to confirm that the isomerization reaction into dihydroxyacetone may occur at low potential. However, the actual HPLC experimental condition made the separation of dihydroxyacetone and glycerate ion difficult due to very close retention times. Also, glycerate ion is the main reaction product at low potentials for this long electrolysis experiment and traces of tartronate have also been detected. The increase of the electrode potential leads to a change in the reaction selectivity toward the production of tartronate and mesoxalate, although glycerate is detected on the whole studied potential range. It is then proposed that glycerol electrooxidation occurs in several steps: the primary alcohol groups are first oxidized into carboxylate, and then the secondary alcohol group of tartronate is oxidized into mesoxalate.

Similar mechanism seems to occur with $Pd_{0.9}Bi_{0.1}/C$ and $Pt_{0.9}Bi_{0.1}/C$ catalysts, but at higher potentials. However, experiments carried out at 0.85 V *vs* RHE on these catalysts also indicate that the C–C bond of mesoxalate could be broken forming oxalate and formiate.

Results obtained from the *in situ* infrared spectroscopy measurements and HPLC combined with chronoamperometry experiments led to propose the mechanism presented in Scheme 1.

4. Conclusion

Nanocatalysts based on palladium, platinum and bismuth have been synthesized by a colloidal route. $Pt_{0.9}Bi_{0.1}/C$, $Pd_{0.9}Bi_{0.1}/C$ and $Pd_{0.45}Pt_{0.45}Bi_{0.1}/C$ nanosized materials have been characterized and their activity toward the glycerol electrooxidation has been investigated by cyclic voltammetry and compared with those of monometallic Pd/C and Pt/C. Several new insights on the synergetic effect between Pd and Pt with Bi were pointed out:

- Bismuth is not alloyed with platinum or palladium, and a low amount of bismuth (lower than 10 at%) is in interaction with the surface of the two other metals.
- The modification of palladium or platinum by bismuth leads to greatly increase the catalytic activity toward glycerol electrooxidation.
- The platinum-free $Pd_{0.9}Bi_{0.1}/C$ catalyst displays the same catalytic activity toward glycerol oxidation as Pt/C.
- The order of activity of catalysts toward glycerol oxidation is $Pd/C < Pt/C = Pd_{0.9}Bi_{0.1}/C < Pt_{0.9}Bi_{0.1}/C = Pd_{0.45}Pt_{0.45}Bi_{0.1}/C$; the replacement of half of the platinum atoms by palladium atoms is possible keeping the same catalytic activity.
- The adsorption of glycerol at low potentials on platinum and platinum catalysts containing bismuth is mainly non-dissociative, leading to low surface poisoning by CO species.
- The modification of palladium and/or platinum surface by bismuth does not change the oxidation mechanism of glycerol; only the potential has an effect on the final product distribution.
- The mechanism seems to involve glycerol adsorption on palladium and/or platinum surface and hydroxyl species formation on bismuth leading to an enhancement of the catalytic activity enhancement through the bifunctional mechanism.

Moreover, electrochemical reactors, either in fuel cell or electrolysis cell configurations, may lead to the co-generation of added value chemicals and electric energy (fuel cell configuration) or hydrogen (electrolysis configuration) by coupling the direct

oxidation of glycerol at the anode side and the reduction of oxygen (fuel cell configuration) or water (electrolysis configuration) at the cathode side. In alkaline medium, noble metal-free catalysts for the oxygen reduction reaction [40,41] and water reduction (hydrogen production) [42] can be used, and alkaline membranes are now commercially available [43–47]. So that, inexpensive non-platinum based catalysts such as transition metal macrocycles can be used to activate the cathode reactions [42,48–50].

Acknowledgement

This work was carried out under the framework of a project (AMELI-0Pt) from the "Programme Interdisciplinaire Energie" of CNRS (French National Centre for Scientific Research).

References

[1] A. Behr, J. Eilting, K. Irawadi, J. Leschinski, F. Lindner, Green Chem. 10 (2008) 13–30.
[2] P. Gallezot, Catal. Today 37 (1997) 405.
[3] S. Carrettin, P. McMorn, P. Johnston, K. Griffin, C.J. Kiely, G.A. Attard, G.J. Hutchings, Top. Catal. 27 (2004) 131.
[4] M. Simões, S. Baranton, C. Coutanceau, Appl. Catal. B 93 (2010) 354–362.
[5] C. Bianchini, P.K. Shen, Chem. Rev. 109 (2009) 4183.
[6] A. Caillard, C. Coutanceau, P. Brault, J. Mathias, J.-M. Léger, J. Power Sources 162 (2006) 66.
[7] C. Coutanceau, S. Brimaud, L. Dubau, C. Lamy, J.-M. Léger, S. Rousseau, F. Vigier, Electrochim. Acta 53 (2008) 6865–6880.
[8] V. Bambagioni, C. Bianchini, A. Marchionni, J. Filippi, F. Vizza, J. Teddy, P. Serp, M. Zhiani, J. Power Sources 190 (2009) 241.
[9] S. Motoo, M. Watanabe, J. Electroanal. Chem. 98 (1979) 203.
[10] M. Shibata, N. Furuya, M. Watanabe, S. Motoo, J. Electroanal. Chem. 263 (1989) 97.
[11] B. Beden, F. Kadirgan, C. Lamy, J.-M. Léger, J. Electroanal. Chem. 142 (1982) 171.
[12] E. Casado-Rivera, D.J. Volpe, L. Alden, C. Lind, C. Downie, T. Vazquez-Alvarez, A. Angelo, F.J. DiSalvo, H. Abruña, J. Am. Chem. Soc. 126 (2004) 4043.
[13] H. Kimura, K. Tsuto, T. Wakisaka, Y. Kazumi, Y. Inaya, Appl. Catal. A 96 (1993) 217.
[14] A. Lopez-Cudero, F. Vidal-Iglesias, J. Solla-Gullon, E. Herrero, A. Aldaz, J.M. Feliu, Phys. Chem. Chem. Phys. 11 (2009) 416.
[15] L. Demarconnay, S. Brimaud, C. Coutanceau, J.-M. Léger, J. Electroanal. Chem. 601 (2007) 169.
[16] J. Clavilier, J.M. Feliu, A. Aldaz, J. Electroanal. Chem. 243 (1988) 419.
[17] I.G. Casella, M. Contursi, Electrochim. Acta 52 (2006) 649.
[18] C. Roychowdhury, F. Matsumoto, V.B. Zeldovich, S.C. Warren, P.F. Mutolo, M. Ballesteros, U. Wiesner, H. Abruña, F.J. DiSalvo, Chem. Mater. 18 (2006) 3365.
[19] W.S. Rasband, Image J, US National Institutes of Health, Bethesda, MA, USA, http://rsbweb.nih.gov/ij/.
[20] F. Gloaguen, N. Andolfatto, R. Durand, P. Ozil, J. Appl. Electrochem. 24 (1994) 863.
[21] B. Molina Concha, M. Chatenet, Electrochim. Acta 54 (2009) 6130.
[22] H. Yano, E. Iguchi, H. Uschida, M. Watanabe, J. Phys. Chem. B 110 (2006) 16544.
[23] B.E. Warren, X-Ray Diffraction, Dover Publications, Inc., NY, 1990.
[24] C.D. Wagner, W.M. Riggs, L.E. Davis, J.F. Moulder, G.E. Mouilenberg (Eds.), Handbook of X-ray Photoelectron Spectroscopy, Perkin-Elmer Corporation, Eden Prairie, MN, 1978.
[25] I.S. Tilinin, A. Jablonski, B. Lesiak-Orlowska, Vacuum 46 (1995) 613–616.
[26] J. Zemek, S. Hucek, A. Jablonski, I.S. Tilinin, J. Electron Spectrosc. Relat. Phenom. 76 (1995) 443–447.
[27] N. Hoshi, N. Nakamura, N. Maki, S. Yamaguchi, A. Kitajima, J. Electroanal. Chem. 624 (2008) 134.
[28] M. Grdeń, M. Łukaszewski, G. Jerkiewicz, A. Czerwiński, Electrochim. Acta 53 (2008) 7583.
[29] U.W. Hamm, D. Kramer, R.S. Zhai, D.M. Kolb, Electrochim. Acta 43 (1998) 2969.
[30] M. Simões, S. Baranton, C. Coutanceau, Electrochim. Acta 56 (2010) 580–591.
[31] Y.Y. Tong, H.S. Kim, P.K. Babu, P. Waszczuk, A. Wieckowski, E. Olfield, J. Am. Chem. Soc. 124 (2002) 468–473.
[32] P. Waszczuk, A. Wieckowski, P. Zelenay, S. Gottesfeld, C. Coutanceau, J.-M. Léger, C. Lamy, J. Electroanal. Chem. 511 (2001) 55–64.
[33] M. Watanabe, S. Motoo, J. Electroanal. Chem. 60 (1975) 275–283.
[34] U.A. Paulus, A. Wokaum, G.G. Scherer, T.J. Schmidt, V. Stamenkovic, N.M. Markovic, P.N. Ross, Electrochim. Acta 47 (2002) 3787–3798.
[35] B.I. Podlovchenko, O.A. Petrii, A.N. Frumkin, H. Lal, J. Electronal. Chem. 11 (1966) 12.
[36] N.W. Smirnova, O.A. Petrii, A. Grzejdziak, J. Electroanal. Chem. 251 (1988) 73.
[37] Y.-X. Jiang, S.-G. Sun, N. Ding, Chem. Phys. Lett. 344 (2001) 463.
[38] C.J. Pouchert, The Aldrich Library of Infrared Spectra, third edition, Aldrich Chemical Company, Inc., Milwaukee, WI, USA, 1981.
[39] D.Z. Jeffery, G.A. Camara, Electrochem. Commun. 12 (2010) 1129.
[40] R. Jamard, J. Salomon, A. Martinent-Beaumont, C. Coutanceau, J. Power Sources 193 (2009) 779.
[41] M. Chatenet, F. Micoud, I. Roche, E. Chainet, Electrochim. Acta 51 (2006) 5452.
[42] Ö.A. Osmanbaş, A. Koca, M. Kandaz, F. Karaca, Int. J. Hydrogen Energy 33 (2008) 3281–3288.
[43] A. Ilie, M. Simões, S. Baranton, C. Coutanceau, S. Martemianov, J. Power Sources 196 (2011) 4965–4971.
[44] H. Hou, G. Sun, R. He, B. Sun, W. Jin, H. Liu, Q. Xin, Int. J. Hydrogen Energy 33 (2008) 7172–7176.
[45] I. Frenzel, H. Holdik, D.F. Stamatialis, G. Pourcelly, M. Wessling, J. Membr. Sci. 261 (2005) 49–57.
[46] H. Yanagi, K. Fukuta, ECS Trans. 16 (2008) 257–262.
[47] K. Fukuta, H. Inoue, Y. Chikashige, H. Yanagi, ECS Trans. 28 (2010) 221–225.
[48] A.D. Modestov, M.R. Tarasevich, A.Y. Leykin, V.Y. Filimonov, J. Power Sources 188 (2009) 502–506.
[49] J. Ma, J. Wang, Y. Liu, J. Power Sources 172 (2007) 220–224.
[50] R. Jamard, J. Salomon, A. Martinent-Beaumont, C. Coutanceau, J. Power Sources 193 (2009) 779–787.